RSC Advances

PAPER

View Article Online
View Journal | View Issue

Cite this: *RSC Adv.*, 2020, **10**, 40276

Effect of $Ti_3C_2T_x$–PEDOT:PSS modified-separators on the electrochemical performance of Li–S batteries†

Juan Li,‡[a] Qi Jin,‡[a] Fei Yin,[a] Chuncheng Zhu,[a] Xitian Zhang *[a] and Zhiguo Zhang [b]

Received 22nd July 2020
Accepted 19th October 2020

DOI: 10.1039/d0ra06380k

rsc.li/rsc-advances

Lithium–sulfur (Li–S) batteries have attracted much attention due to their high theoretical energy density, environmental friendliness, and low cost. However, the practical application of Li–S batteries is impeded by a severe shuttle effect. Using polar and conductive materials to prepare a modified separator as the second collector is an effective strategy to solve the shuttle effect. Herein, a $Ti_3C_2T_x$–PEDOT:PSS hybrid for modifying PP separators is successfully fabricated. In this hybrid, PEDOT:PSS can effectively prevent $Ti_3C_2T_x$ nanosheets from restacking and enhance the electrical conductivity of Li–S batteries, thereby promoting fast Li^+/electron transport and improving the sulfur utilization. Meanwhile, the introduction of $Ti_3C_2T_x$–PEDOT:PSS makes $Ti_3C_2T_x$ nanosheets effectively anchor polysulfide, thus inhibiting the shuttle effect. As a result, Li–S cells with $Ti_3C_2T_x$–PEDOT:PSS modified-separators exhibit superior performances, including a high discharge capacity of 1241.4 mA h g^{-1} at 0.2C, a long cycling stability, and a low decay rate of 0.030% per cycle at 0.5C for 1000 cycles.

Introduction

Lithium–sulfur (Li–S) batteries are the most promising energy storage system due to their high theoretical energy density (2570 W h kg^{-1}), environmental friendliness, and low cost.[1–4] Nevertheless, the practical application of Li–S batteries still suffers from many challenges. For example, lithium polysulfides (LiPSs) dissolve in ether-based electrolytes, leading to a severe shuttle effect, which gives rise to a significant change in the structure of the cathode, inferior stability of the anode, low coulombic efficiency, and loss of active materials.[5–11] In the past years, researchers have solved this problem by designing nanostructured scaffolds of sulfur to improve the electrical conductivity of the cathode and confine lithium polysulfides (LiPSs).[12–14] Although the shuttle effect has been significantly improved, the dissolution of LiPSs is inevitable in ether-based liquid electrolytes. Besides, optimizing electrolytes and constructing multifunctional interlayer are also used to improve the shuttle effect.[15,16] In which, introducing an interlayer between the cathode and the separator is an effective approach. It can serve as the second collector to enhance the cathode conductivity and provide LiPS confinement to diminish LiPS shuttling simultaneously. In 2012, Manthiram and co-workers firstly applied porous carbon interlayers to improve sulfur utilization and mitigate the shuttle effect of LiPSs. The cell delivered a high capacity more than 1000 mA h g^{-1} for 100 cycles at a current density of 1C.[17] However, the weak interaction between non-polar carbon materials and polar LiPSs cannot effectively immobilize LiPSs, inevitably resulting in serious capacity decay during long-term cycling. For this reason, some attentions have been paid to modify PP separators by using various polar materials, such as heteroatom-doped carbons,[18,19] metal oxides,[20–22] and metal sulfides,[23–25] which can strongly interact with LiPSs and effectively mitigate the diffusion of LiPSs. However, the poor electronic conductivity of these compounds is harmful to achieve high initial capacity and cause high battery polarization. Thus, exploration of polar materials simultaneously with excellent conductivity property and strong LiPS adsorption ability to modify separators is of great significance for enhancing the cycling performance of Li–S batteries.

$Ti_3C_2T_x$, as a representative MXene material has a unique 2D structure, and rich surface functional groups.[26,27] Nazar group demonstrated for the first time that $Ti_3C_2T_x$ could effectively entrap LiPSs and promote them conversion *via* the double mechanism of Lewis acid–base interaction and thiosulfate/polythionate disproportionation.[28] In 2018, $Ti_3C_2T_x$ nanosheets were used as sulfur host materials. The assembled cell exhibited a high initial discharge capacity of 1458 mA h g^{-1} at 0.1 A g^{-1} and an ultralow capacity loss of 0.04% per cycle at 0.8 A g^{-1} over 1500 cycles.[16] In addition, Wang and coworker

[a]*Laboratory for Photonic and Electronic Bandgap Materials, Ministry of Education, School of Physics and Electronic Engineering, Harbin Normal University, Harbin 150025, People's Republic of China. E-mail: xtzhangzhang@hotmail.com*

[b]*Condensed Mater Science and Technology Institute, Department of Physics, Harbin Institute of Technology, Harbin 150001, People's Republic of China*

† Electronic supplementary information (ESI) available. See DOI: 10.1039/d0ra06380k

‡ These authors contributed equally to this work.

employed $Ti_3C_2T_x$ nanosheet-modified PP separator to improve electric conductivity and effectively trap LiPSs in Li–S batteries, which delivered a reversible capacity of 550 mA h g^{-1} with a capacity decay of only 0.062% per cycle at 0.5C after 500 cycles.[29] Above reports confirmed that the $Ti_3C_2T_x$ nanosheets can effectively anchor LPSs and improve the electrical conductivity of cathode. However, the restacking issue of 2D layer-structure MXenes still remains, which limits the ion transport and reduces the available active surface. Polymers, as a special class of interlayer spacer materials, are widely applied in MXene-based supercapacitor to prevent MXene nanosheets from restacking, thereby facilitating fast Li^+/electron transfer and achieving excellent electrochemical performance.[30] Among many polymers, PEDOT:PSS shows great advantages due to its excellent mechanical flexibility, low cost, and commercial availability.[31] Therefore, combining PEDOT:PSS with 2D active $Ti_3C_2T_x$ to modify separators will be a promising strategy to obtain high-capacity and long-life Li–S batteries.

Herein, $Ti_3C_2T_x$–PEDOT:PSS (labelled as $Ti_3C_2T_x$–P) hybrid was successfully synthesized and employed it to modify PP separators (labelled as $Ti_3C_2T_x$–P separators). The cell with the $Ti_3C_2T_x$–P separator exhibited a high initial discharge capacity of 1241.4 mA h g^{-1} at a current density of 0.2C and retains 955.2 mA h g^{-1} after 100 cycles. Importantly, it showed an ultra-low capacity decay rate of 0.030% per cycle with a reversible discharge capacity of 485.3 mA h g^{-1} at 0.5C for over 1000 cycles, revealing the outstanding cycling stability.

Experimental section

Fabrication of $Ti_3C_2T_x$–P separators

The $Ti_3C_2T_x$ suspension was prepared *via* a typical method[32] and the mixed solution of $Ti_3C_2T_x$ and commercial PEDOT:PSS was synthesized as follows: 10 mL of $Ti_3C_2T_x$ suspension (1.5 mg mL^{-1}) and different volumes of commercial PEDOT:PSS solution (1 g mL^{-1}) were mixed and stirred for 1 h to obtain a homogeneous solution. The volume of commercial PEDOT:PSS solution is 25, 50, 100, 500, and 1000 μL, and their corresponding mass is 0.375, 0.75, 1.5, 7.5, and 15.0 mg, *i.e.* The content of PEDOT:PSS in $Ti_3C_2T_x$–P composite materials is 2.4, 4.8, 9.1, 33.3 and 50.0 wt%, respectively. Then the mixture was frozen at −80 °C for 2 h and subsequently the remaining water in the as-frozen sediments was removed by using a freeze-drying technology. $Ti_3C_2T_x$–P separator was fabricated by mixing 90 wt% of $Ti_3C_2T_x$–P composites, 10 wt% of polyvinylidene fluoride (PVDF) in the *N*-methyl-2-pyrrolidone (NMP) solvent. After continuously ultrasound for 30 min, the homogeneous suspension was deposited onto the PP separator *via* vacuum filtration. The obtained $Ti_3C_2T_x$–P separator was dried in a vacuum oven at 60 °C overnight and cut into individual pieces with a diameter of 19 mm. The mass loading of $Ti_3C_2T_x$–P is about 0.8 mg cm^{-2}. The $Ti_3C_2T_x$-modified separator was prepared according to the same procedure.

Preparation of C/S cathode

C/S composites were prepared *via* a simple ball-milling process. The weight ratio of active carbon and sublimed sulfur was 1 : 3. Afterwards, this mixture was heated at 155 °C for 12 h in a sealed vessel to ensure enough infusion of the molten sulfur. To prepare the C/S cathode, active carbon, carbon black (CB), and PVDF (8 : 1 : 1 by weight) were further ball milled in NMP to form a homogeneous slurry. The slurry was directly coated onto aluminum foil as a current collector by using a doctor blade. The obtained film was dried in a vacuum oven at 60 °C for 12 h, and cut into individual pieces with a diameter of 13 mm. The areal sulfur loading in the C/S cathode is 1.0–1.2 mg cm^{-2}.

Preparation of Li_2S_6 solution

Sulfur and lithium sulfide (Li_2S, 99.9%, Sigma-Aldrich) with a molar ratio of 5 : 1 was added into 1,2-dimethoxyethane (DME) and 1,3-dioxolane (DOL) (1 : 1 by volume) by magnetically stirring for 12 h in a confined environment to form Li_2S_6 solution (0.01 M). All procedures were performed under an Ar atmosphere.

Electrochemical tests

Stainless steel coin cells (CR2025) were assembled in an argon-filled glove box using the C/S cathode, Li metal foil anode, and modified separator with the $Ti_3C_2T_x$–P layer facing the C/S cathode. In this experiment, the electrolyte (30 μL) is composed of 1.0 M lithium bis(trifluoromethanesulfonyl)imide (LiTFSI) and 0.2 M $LiNO_3$ in the mixture of DOL/DME (1 : 1, v/v). The other cells with the $Ti_3C_2T_x$-modified and blank separators were assembled *via* the same procedure.

The galvanostatic charge–discharge performance (GCD) was tested on a LANCT battery program-control test system (Wuhan, China) in a potential range between 1.7–2.8 V at room temperature. The cyclic voltammetry (CV) curves were measured on a VMP3 electrochemical workstation (BioLogic, France) in a potential range of 1.7–2.8 V (Li/Li^+) at a scan rate of 0.1 mv s^{-1}. The electrochemical impedance spectroscopy (EIS) measurements were conducted in a frequency range from 10 mHz to 100 kHz.

Structural characterizations

The morphologies of $Ti_3C_2T_x$ and $Ti_3C_2T_x$–P hybrid were observed by scanning electron microscopy (SEM, SU70, Hitachi, Japan), X-ray diffraction (XRD, D/max2600, Rigaku, Japan, Cu Kα radiation, $\lambda = 1.5418$ Å) and transmission electron microscopy (TEM, FEI, Tecnai TF20) were used to characterize the crystal structure of the samples. An analysis of the specific surface area and pore volume of the samples were performed using an automatic N_2 adsorption–desorption instrument (ASAP 2010, Micromeritics). The element composition of the samples was analyzed by an X-ray photoelectron spectroscopy (XPS, K-alpha X-ray spectrometer, Thermo Scientific Company). Raman spectra were conducted by a Micro-Raman spectrometer (J-Y; HR800, France) under an excitation wavelength of 488 nm. Fourier transform infrared (FT-IR) spectra were obtained using

a Magna Model 560 FT-IR spectrometer with a resolution of 1 cm^{-1}. The electrical conductivity was measured using Hall (HL5550LN2, CRYOSTAT, USA).

Results and discussion

Digital photos of $Ti_3C_2T_x$ and a representative $Ti_3C_2T_x$–P modified separators were taken, as shown in Fig. S1.† The surface of the PP separators was uniformly covered by $Ti_3C_2T_x$ and $Ti_3C_2T_x$–P after vacuum filtration. The surface of the $Ti_3C_2T_x$–P modified separator becomes blacker and denser than that of the $Ti_3C_2T_x$ modified separator. Top-view SEM images of both $Ti_3C_2T_x$-modified separator and $Ti_3C_2T_x$–P separator are shown in Fig. 1a–d, respectively. The mass loadings of $Ti_3C_2T_x$ and $Ti_3C_2T_x$–P are the same on PP separators. As shown in Fig. 1a and b, the $Ti_3C_2T_x$ and $Ti_3C_2T_x$–P modified separators show relatively sparse surface morphology. In contrast, the cross-sectional thickness of $Ti_3C_2T_x$–P separator (49.7 μm) is 1.8 times higher than that of $Ti_3C_2T_x$ (~27.1 μm) after introducing PEDOT:PSS (Fig. 1c and d). The elemental mapping of $Ti_3C_2T_x$–P on the PP separator was conducted to illustrate the homogeneous distribution of PEDOT:PSS on the $Ti_3C_2T_x$ surface (Fig. S2†). Moreover, the specific surface area and pore volume of the $Ti_3C_2T_x$–P (96.9 m^2 g^{-1}, 0.255 cm^3 g^{-1}) were also higher than that of the stacked $Ti_3C_2T_x$ (18.2 m^2 g^{-1}, 0.061 cm^3 g^{-1}) (Fig. S3†), indicating a larger accessible active surface area of

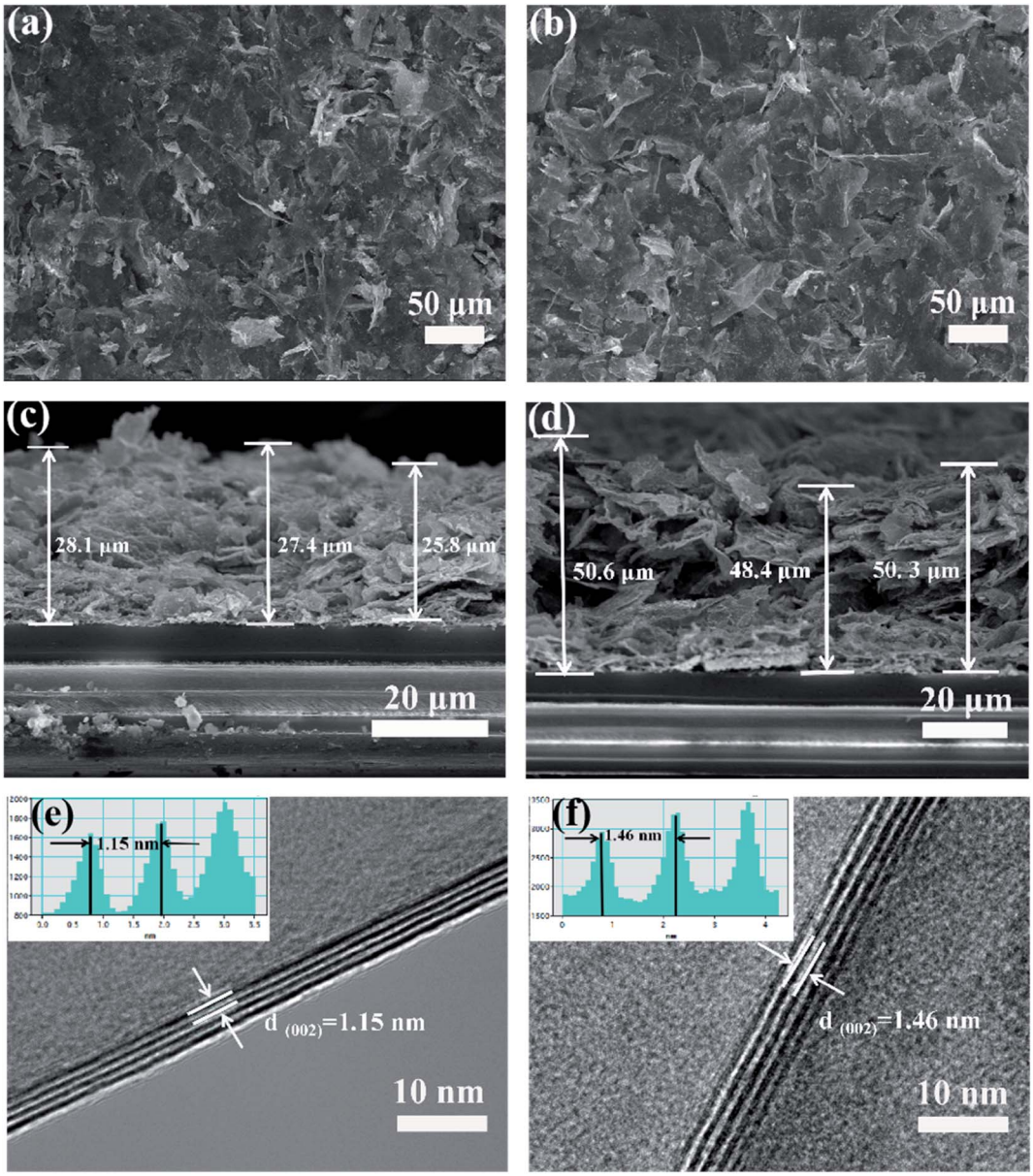

Fig. 1 Top-view SEM images of (a) pure $Ti_3C_2T_x$-modified and (b) $Ti_3C_2T_x$–P separators. Cross-sectional SEM images of the (c) $Ti_3C_2T_x$-modified and (d) $Ti_3C_2T_x$–P separators. HRTEM images of (e) $Ti_3C_2T_x$ nanosheet and (f) $Ti_3C_2T_x$–P nanosheet (inset is a profile plot of the calibration for measuring the spacing of $Ti_3C_2T_x$).

$Ti_3C_2T_x$–P. Besides, according to the high-resolution transmission electron microscopy (HRTEM) images (Fig. 1e and f), the interlayer spacing of the (002) plane of $Ti_3C_2T_x$ nanosheets in $Ti_3C_2T_x$–P is 14.6 Å, much larger than that of $Ti_3C_2T_x$ (11.5 Å), further confirming that PEDOT:PSS has been successfully intercalated between the adjacent $Ti_3C_2T_x$ layers and the interlayer distance is significantly increased.

The XRD patterns of $Ti_3C_2T_x$ and $Ti_3C_2T_x$–P were also measured, further confirming the changes in interlayer spacing observed by HRTEM. The (002) peak (Fig. 2a) located at around 7.5° for pure $Ti_3C_2T_x$ corresponds to the interlayer spacing of 11.7 Å. However, the (002) peak (Fig. 2b) of the $Ti_3C_2T_x$ in $Ti_3C_2T_x$–P shifts to a lower diffraction angle of ~5.9°, corresponding to the interlayer spacing of 14.9 Å, indicating that the interlayer spacing has increased by ~3.2 Å, which is consistent with the HRTEM results. $Ti_3C_2T_x$ and $Ti_3C_2T_x$–P composites were also characterized by Raman and FT-IR spectra. The strong Raman peaks at 1372 cm^{-1} and 1574 cm^{-1} (Fig. 2c) correspond to the D-band and G-band of the crystalline graphite carbon due to the exposed C on the surface of $Ti_3C_2T_x$.[30] In addition, the bands at 995, 1199, 1262, 1433, 1558 cm^{-1} are attributed to oxyethylene ring deformation, quinoid ring vibration, Cá–Cá stretching vibrations, C=C symmetric stretching, and antisymmetric Cá–Cá stretching deformations in PEDOT:PSS.[33–35] All characteristic peaks shown in $Ti_3C_2T_x$–P indicate that PEDOT:PSS has been successfully intercalated between adjacent $Ti_3C_2T_x$ layers. This result was further confirmed by the FT-IR spectra, as shown in Fig. 2d. C–O (~1051 cm^{-1}), C–F (~1089 cm^{-1}), C–C (~1402 cm^{-1}), and –OH (~1639 cm^{-1}) groups originate from the characteristic peaks of pure $Ti_3C_2T_x$.[30]

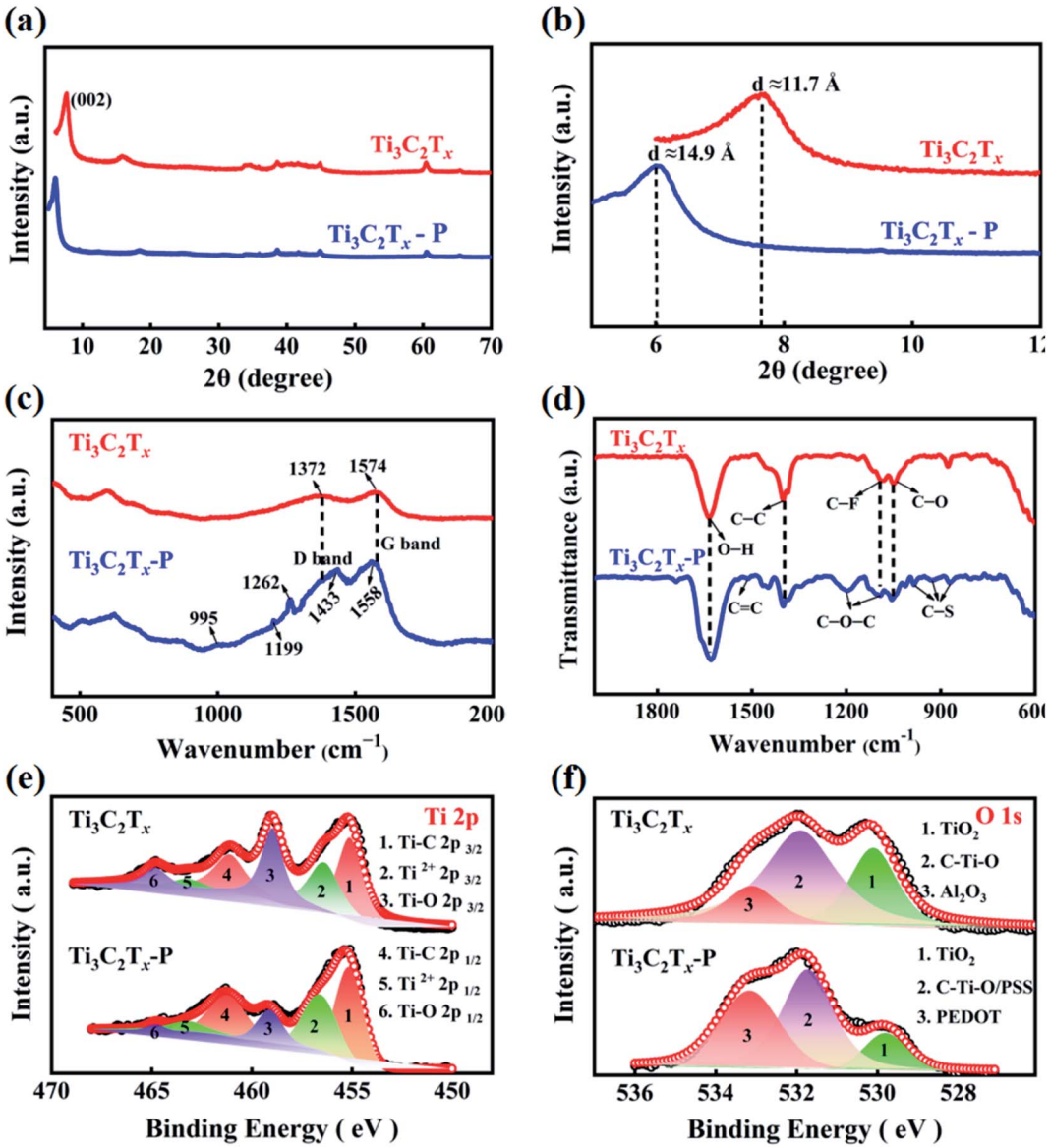

Fig. 2 (a) XRD patterns of $Ti_3C_2T_x$ and $Ti_3C_2T_x$–P and (b) corresponding enlarged XRD patterns. (c) Raman spectra and (d) FTIR spectra of $Ti_3C_2T_x$ and $Ti_3C_2T_x$–P. XPS spectra of (e) Ti 2p and (f) O 1s of $Ti_3C_2T_x$ and $Ti_3C_2T_x$–P.

The band at 1509 cm^{-1} is related to the C=C stretching of the thiophene rings in PEDOT,[36] while the bands at 1201 cm^{-1} and 1094 cm^{-1} are attributed to the C–O–C bond stretching of the ethylenedioxy group.[37] Meanwhile, the IR bands at 988, 926 and 870 cm^{-1} correspond to the C–S stretching mode.[38] These peaks belong to the characteristic peaks of PEDOT:PSS. From Fig. 2d, $Ti_3C_2T_x$–P is composed of the $Ti_3C_2T_x$ and PEDOT:PSS, suggesting the successful intercalation of PEDOT:PSS between adjacent $Ti_3C_2T_x$ layers. Above SEM, TEM, XRD, Raman and FT-IR results suggest that the addition of PEDOT:PSS can increase the interlayer spacing of $Ti_3C_2T_x$ and effectively prevent the restacking phenomenon, which is beneficial to promote Li^+/electron transport for rapid sulfur conversion and expose more active sites to adsorb LiPSs, thereby reducing the diffusion of LiPSs in the electrolyte and improving the electrochemical performance of Li–S batteries during cycling processes. XPS measurements were carried out to investigate the elemental composition and chemical bonding states of the $Ti_3C_2T_x$ and $Ti_3C_2T_x$–P, and the detailed peak assignments and interpretation are provided in Fig. S4 and Table S1.† Compared with pure $Ti_3C_2T_x$, the peaks of Ti–C and Ti–O bonds for the Ti $2p_{3/2}$ state in $Ti_3C_2T_x$–P shift to a higher binding energy of ~0.4 eV[39,40] (Fig. 2e), whereas the S $2p_{3/2}$ and S $2p_{1/2}$ states of the PEDOT chain in $Ti_3C_2T_x$–P shift to a lower binding energy of ~0.6 eV[41] (Fig. S3b†). Meanwhile, the O 1 s spectrum for $Ti_3C_2T_x$–P shows a negative shift of ~0.2 eV[39] (Fig. 2f). These shifts of binding energy are attributed to the charge transfer interaction between $Ti_3C_2T_x$ and PEDOT:PSS. The electrons transferred to $Ti_3C_2T_x$ enhance the strength of the originally weakened Ti–C bond by $Ti_3C_2T_x$ surface groups, thereby improving the electrical conductivity of $Ti_3C_2T_x$.[39,42] This result is further proved by Hall measurements, as shown in Table S2.† $Ti_3C_2T_x$–P possesses higher conductivity of 3.19 S cm^{-1} than that of $Ti_3C_2T_x$ (1.66 S cm^{-1}), which is beneficial to promote the charge transport kinetics and obtain a high discharge specific capacity during the cycling processes.

In order to investigate the electrochemical performance of Li–S cells with $Ti_3C_2T_x$–P separator, CR2025 coin cells were assembled, using C/S composites as the cathode, lithium metal foil as the anode. The cycling performance of the cells using $Ti_3C_2T_x$–P separators with different amounts of PEDOT:PSS (2.4, 4.8, 9.1, 33.3 and 50.0 wt%) is shown in Fig. S5.† By comparison, the cell with 9.1 wt% PEDOT:PSS exhibits the highest specific capacity of 1226.2 mA h g^{-1} and the best cycle stability at 0.5C. Therefore, subsequent experiments were performed, using $Ti_3C_2T_x$–P separator with 9.1 wt% PEDOT:PSS. Meanwhile, the cells with blank separator and $Ti_3C_2T_x$-modified separator were also assembled for comparison. Fig. 3a shows the CV curves of the cells with blank, $Ti_3C_2T_x$-modified and $Ti_3C_2T_x$–P separators at 0.1 mV s^{-1} and in a voltage ranging of 1.7–2.8 V. All cells show two cathodic peaks (i and ii), corresponding to the typical multistep reductions from sulfur to soluble long-chain LiPSs (Li_2S_x, $4 \leq x \leq 8$) and then to insoluble short-chain Li_2S_2/Li_2S. While the anodic peaks (iii and iv) are attributed to the conversion of Li_2S/Li_2S_2 to LiPSs, and further conversion to sulfur. By comparison, all peak intensities of the cells with $Ti_3C_2T_x$–P separator are higher than those of the cells with other separators, implying the increased utilization of active materials. More importantly, the CV curves (Fig. 3b) of the cell with $Ti_3C_2T_x$–P separator are almost consistent from the first to the fifth cycle, implying the remarkable cycling stability and high reversibility. The GCD voltage profiles of the cells with blank, $Ti_3C_2T_x$-modified and $Ti_3C_2T_x$–P separators are investigated at a current density of 0.2C, as shown in Fig. 3c. Two typical voltage platforms of these cells are observed in the discharge profile, which is in good agreement with the CV curves. The cells with the blank, $Ti_3C_2T_x$-modified and $Ti_3C_2T_x$–P separators exhibit initial specific capacities of 866.0 mA h g^{-1}, 1039.3 mA h g^{-1} and 1241.4 mA h g^{-1}, respectively, and remain the corresponding 571.0 mA h g^{-1}, 600.1 mA h g^{-1} and 955.2 mA h g^{-1} after 100 cycles (Fig. 3c and d), indicating that the cell with $Ti_3C_2T_x$–P separator has an increased utilization of sulfur again. In addition, EIS measurements were also performed to evaluate the electrical conductivity of cells, as shown in Fig. 3e. The charge transfer resistance (R_{ct}) of the cell with $Ti_3C_2T_x$–P separator is much lower than that of the cells with the blank and $Ti_3C_2T_x$-modified separators, indicating that the introduction of PEDOT:PSS can enhance the conductivity of cell, which can improve the electron transfer for fast redox reaction kinetics. To compare the anchoring performance of $Ti_3C_2T_x$ and $Ti_3C_2T_x$–P in Li_2S_6, $Ti_3C_2T_x$ and $Ti_3C_2T_x$–P were added into 0.01 M Li_2S_6 solution, respectively, and then stood for 30 min. As shown in the inset of Fig. 3f, Li_2S_6 solution with $Ti_3C_2T_x$–P fades into colorless, while another solution is still lightly yellow, indicating that $Ti_3C_2T_x$–P has the superior absorption ability of LiPSs. In addition, the UV-vis spectrum was used to assess the absorbing Li_2S_6 ability of $Ti_3C_2T_x$ and $Ti_3C_2T_x$–P, as shown in Fig. 3f. Obviously, the absorbing Li_2S_6 ability of $Ti_3C_2T_x$–P is the best, which is in agreement with the above observation. All above results indicate that the combining of $Ti_3C_2T_x$ and PEDOT:PSS can improve the conductivity of $Ti_3C_2T_x$, expose more active sites to anchor LiPSs and improve the utilization of sulfur.

Fig. 4a and b shows the rate performance of the cells with different separators. The cell with $Ti_3C_2T_x$–P separator displays the best rate performance, and delivers corresponding discharge capacities of 1438.4, 1102.8, 846.6, 715.6, and 607.9 mA h g^{-1} at 0.1, 0.2, 0.5, 1.0, and 2.0C, respectively. When the current densities return to 0.2 and 0.1C, the discharge capacities of 1065.4 and 1273.6 mA h g^{-1} are retained, corresponding to 96.6% and 88.5% of the initial capacity. These results indicate that $Ti_3C_2T_x$–P separator is beneficial to promote excellent reversibility and enhance high sulfur utilization. However, the cell with $Ti_3C_2T_x$-modified separator shows slightly worse discharge capacity of 763.1 and 949.6 mA h g^{-1} when the current densities switches back to 0.2 and 0.1C, because the restacking phenomenon affects the adsorption capacity of $Ti_3C_2T_x$. By comparison, the cell with blank separator displays the worst rate performance and the fastest capacity decay from 907.7 mA h g^{-1} at 0.1C to 150.2 mA h g^{-1} at 2C. In addition, the GCD profiles of the cell with $Ti_3C_2T_x$–P separator (Fig. S6†) at high rates shows much flatter and more stable plateaus compared to blank and $Ti_3C_2T_x$-modified separator, demonstrating superior rate performance and high

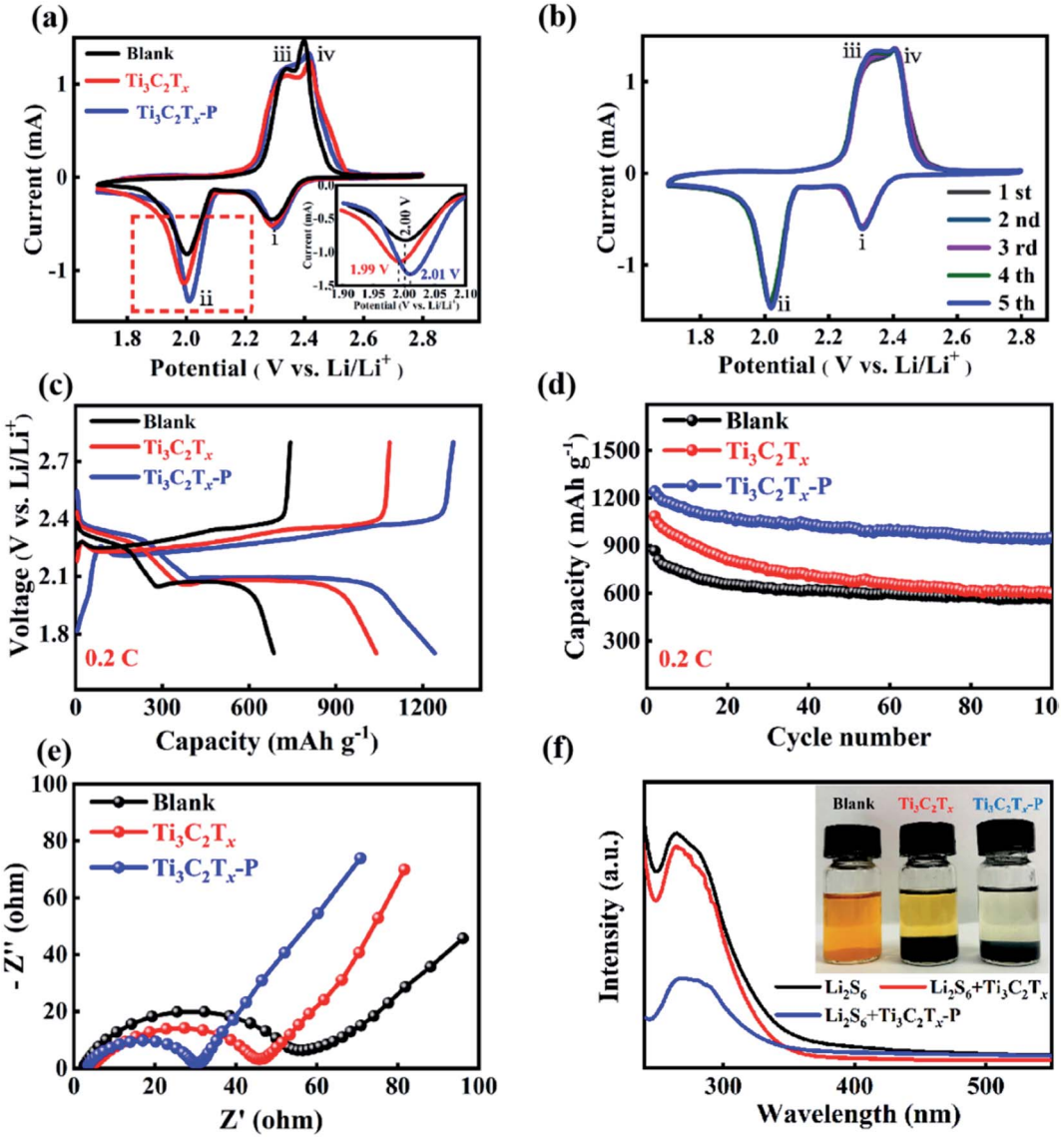

Fig. 3 CV curves of the cells with (a) blank, $Ti_3C_2T_x$-modified, and $Ti_3C_2T_x$–P separators, respectively, and (b) $Ti_3C_2T_x$–P separator cycled at a scan rate of 0.1 mV s^{-1}. (c) Charge–discharge profiles of the cells with blank, $Ti_3C_2T_x$-modified, and $Ti_3C_2T_x$–P separators at 0.2C. (d) Cycling performance of the cells with blank, $Ti_3C_2T_x$-modified, and $Ti_3C_2T_x$–P separators at 0.2C. (e) EIS spectra of the cells with blank, $Ti_3C_2T_x$-modified, and $Ti_3C_2T_x$–P separators. (f) UV-vis absorption spectra of pure Li_2S_6 solution and the solution containing $Ti_3C_2T_x$ and $Ti_3C_2T_x$–P. Inset shows their corresponding digital photos for each solution.

electrochemical reversibility. The cycling stability of Li–S cells with blank, $Ti_3C_2T_x$-modified and $Ti_3C_2T_x$–P separators were also tested at 0.5C, as shown in Fig. 4c. The initial discharge capacities of blank, $Ti_3C_2T_x$-modified and $Ti_3C_2T_x$–P separators are 434.8, 1046.4 and 1182.1 mA h g^{-1}, respectively. After 1000 cycles, a high reversible discharge capacity of 485.3 mA h g^{-1} is retained for $Ti_3C_2T_x$–P separators with an ultralow capacity fade rate as low as 0.030% per cycle, indicating the strong anchoring LiPS ability of $Ti_3C_2T_x$–P. The corresponding GCD profiles of the cell is shown in Fig. S7.† However, after 400 cycles, the cell with $Ti_3C_2T_x$ separators displays fast capacity decay from 1046.4 mA h g^{-1} to 432.3 mA h g^{-1} due to the weak chemisorption of LiPSs by $Ti_3C_2T_x$ alone, while the blank separator only preserves 343.3 mA h g^{-1}. Obviously, the cell with $Ti_3C_2T_x$–P separator has a higher initial discharge capacity and a lower decay rate. In order to observe the morphology of the separator after cycling, SEM images of $Ti_3C_2T_x$ and $Ti_3C_2T_x$–P modified separators after 30 cycles at 0.5C are shown in Fig. S8.† Compared with $Ti_3C_2T_x$ separator, the $Ti_3C_2T_x$–P separator shows a denser surface due to more Li_2S deposition. The obtained good performance could be attributed to the advantages of $Ti_3C_2T_x$–P separator as follows: (i) the introduction of PEDOT:PSS can enhance the electrical conductivity of the cell and effectively prevent $Ti_3C_2T_x$ nanosheets from restacking, thereby promoting fast Li^+/electron transport. (ii) $Ti_3C_2T_x$–P hybrid with high active surface can chemically anchor LiPSs, promote them conversion, improve the sulfur utilization, and effectively inhibit the shuttle effect.

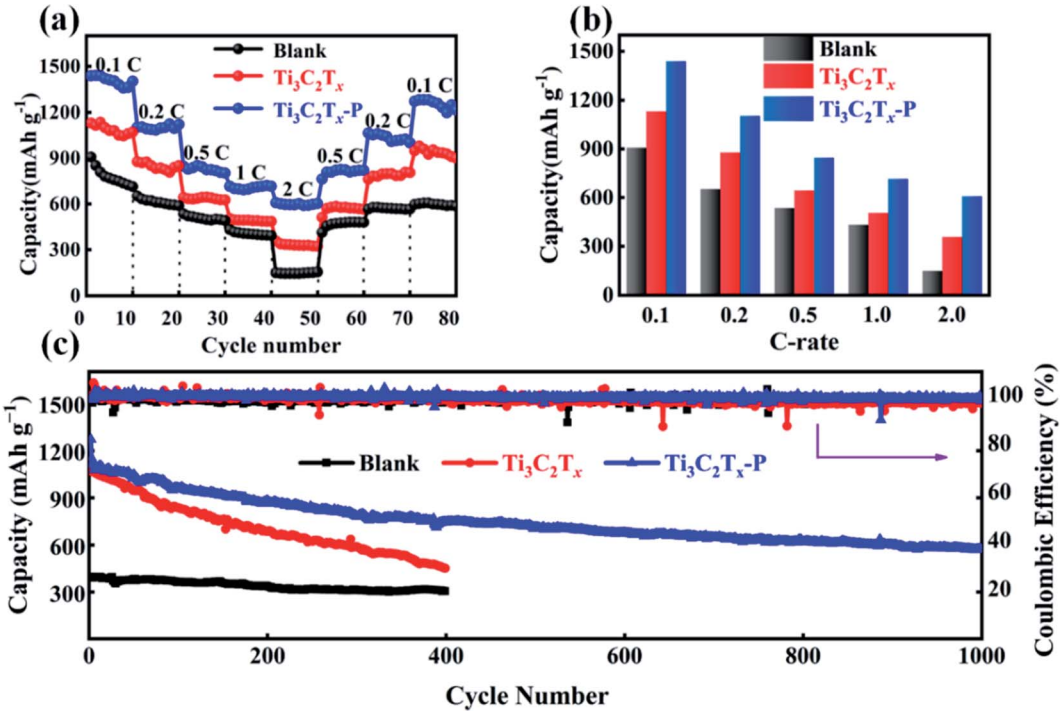

Fig. 4 (a) Rate performance of the cells with blank, $Ti_3C_2T_x$-modified, and $Ti_3C_2T_x$–P as separators. (b) Histogram of charge–discharge curves of blank, $Ti_3C_2T_x$-modified and $Ti_3C_2T_x$–P at different C rates. (c) Long-term cycling performance and coulombic efficiency of the cells with blank, $Ti_3C_2T_x$-modified, and $Ti_3C_2T_x$–P separators at 0.5C for 1000 cycles.

Conclusions

In summary, $Ti_3C_2T_x$–P separators were rationally designed and successfully prepared to achieve high performance Li–S batteries. On the one hand, the introduction of PEDOT:PSS enhances the electrical conductivity of Li–S batteries and effectively prevents $Ti_3C_2T_x$ from restacking, thereby promoting fast Li^+/electron transport. On the other hand, $Ti_3C_2T_x$–P with high active surface has a strong anchoring effect to LiPSs to suppress the shuttle effect, thereby improving the cycling and rate performance of Li–S batteries. With these advantages, Li–S batteries with $Ti_3C_2T_x$–P separator achieve an excellent electrochemical performance. This work could provide an outstanding strategic guidance on designing modified separator for cycling stability Li–S batteries.

Conflicts of interest

There are no conflicts to declare.

Acknowledgements

This work was partly supported by National Natural Science Foundation of China (51772069).

References

1 H. J. Peng, J. Q. Huang, X. B. Cheng and Q. Zhang, *Adv. Energy Mater.*, 2017, **7**, 1700260.
2 W. B. Kong, L. J. Yan, Y. F. Luo, D. T. Wang, K. L. Jiang, Q. Q. Li, S. S. Fan and J. P. Wang, *Adv. Funct. Mater.*, 2017, **27**, 1606663.
3 S. H. Chung and A. Manthiram, *Adv. Mater.*, 2014, **26**, 1360–1365.
4 Y. Zhong, D. L. Chao, S. J. Deng, J. Y. Zhan, R. Y. Fang, Y. Xia, Y. D. Wang, X. L. Wang, X. H. Xia and J. P. Tu, *Adv. Funct. Mater.*, 2018, **28**, 1706391.
5 Q. Jin, X. T. Zhang, H. Gao, L. Li and Z. G. Zhang, *J. Mater. Chem. A*, 2020, **8**, 8979–8988.
6 S. H. Shen, X. H. Xia, Y. Zhong, S. J. Deng, D. Xie, B. Liu, Y. Zhang, G. X. Pan, X. L. Wang and J. P. Tu, *Adv. Mater.*, 2019, **31**, 1900009.
7 N. Li, Z. X. Chen, F. Chen, G. J. Hu, S. G. Wang, Z. H. Sun, X. D. Sun and F. Li, *Carbon*, 2019, **143**, 523–530.
8 L. L. Zhang, X. Chen, F. Wan, Z. Q. Niu, Y. J. Wang, Q. Zhang and J. Chen, *ACS Nano*, 2018, **12**, 9578–9586.
9 H. J. Peng, J. Q. Huang and Q. Zhang, *Chem. Soc. Rev.*, 2017, **46**, 5237–5288.
10 X. N. Tang, Z. H. Sun, H. C. Yang, H. T. Fang, F. Wei, H. M. Cheng, S. P. Zhuo and F. Li, *J. Energy Chem.*, 2019, **31**, 119–124.
11 F. Yin, Q. Jin, H. Gao and X. T. Zhang, *J. Energy Chem.*, 2021, **53**, 340–346.
12 Z. Li, H. B. Wu and X. W. Lou, *Energy Environ. Sci.*, 2016, **9**, 3061–3070.
13 J. H. Peng and Q. Zhang, *Angew. Chem., Int. Ed.*, 2015, **54**, 11018–11020.

14 C. L. Dai, J. M. Lim, M. Q. Wang, L. Y. Hu, Y. M. Chen, Z. Y. Chen, H. Chen, S. J. Bao, B. L. Shen, Y. Li, G. Henkelman and M. W. Xu, *Adv. Funct. Mater.*, 2018, **28**, 1704443.
15 M. M. Liu, X. Chen, C. G. Chen, T. Y. Ma, T. Huang and A. S. Yu, *J. Power Sources*, 2019, **424**, 254–260.
16 Q. Jin, N. Zhang, C. C. Zhu, H. Gao and X. T. Zhang, *Nanoscale*, 2018, **10**, 16935–16942.
17 Y. S. Su and A. Manthiram, *Nat. Commun.*, 2012, **3**, 1166.
18 L. B. Ma, H. Yuan, W. J. Zhang, G. Y. Zhu, Y. R. Wang, Y. Hu, P. Y. Zhao, R. P. Chen, T. Chen, J. Liu, Z. Hu and Z. Jin, *Nano Lett.*, 2017, **17**, 7839–7846.
19 R. P. Fang, A. Y. Zhao, Z. H. Sun, D. W. Wang, R. Amal, S. G. Wang, H. M. Cheng and F. Li, *Energy Storage Mater.*, 2018, **10**, 56–61.
20 L. B. Ma, R. P. Chen, G. Y. Zhu, Y. Hu, Y. R. Wang, T. Chen, J. Liu and Z. Jin, *ACS Nano*, 2017, **11**, 7274–7283.
21 Y. Guo, Y. Zhang, Y. Zhang, M. W. Xiang, H. Wu, H. K. Liu and S. X. Dou, *J. Mater. Chem. A*, 2018, **6**, 19358–19370.
22 J. R. He, L. Luo, Y. F. Chen and A. Manthiram, *Adv. Mater.*, 2017, **29**, 1702707.
23 X. Liu, J. Q. Huang, Q. Zhang and L. Q. Mai, *Adv. Mater.*, 2017, **29**, 1601759.
24 S. Z. Wang, H. Y. Chen, J. X. Liao, Q. Sun, F. P. Zhao, J. Luo, X. T. Lin, X. B. Niu, M. Q. Wu, R. Y. Li and X. L. Sun, *ACS Energy Lett.*, 2019, **4**, 755–762.
25 J. Xu, W. X. Zhang, H. B. Fan, F. L. Cheng, D. W. Su and G. X. Wang, *Nano Energy*, 2018, **51**, 73–82.
26 M. Naguib, V. N. Mochalin, M. W. Barsoum and Y. Gogotsi, *Adv. Mater.*, 2014, **26**, 992–1005.
27 Q. Jin, L. Li, H. R. Wang, H. Gao, C. C. Zhu and X. T. Zhang, *Electrochim. Acta*, 2019, **312**, 149–156.
28 X. Liang, Y. Rangom, C. Y. Kwok, Q. Pang and L. F. Nazar, *Adv. Mater.*, 2016, **29**, 1603040.
29 J. J. Song, D. W. Su, X. Q. Xie, X. Guo, W. Z. Bao, G. J. Shao and G. X. Wang, *ACS Appl. Mater. Interfaces*, 2016, **8**, 29427–29433.
30 L. Li, N. Zhang, M. Y. Zhang, X. T. Zhang and Z. G. Zhang, *Dalton Trans.*, 2018, **48**, 1747–1756.
31 R. W. Yi, X. F. Lin, Y. C. Zhao, C. G. Liu, Y. Q. Li, L. J. Hardwick, L. Yang, C. Z. Zhao, X. W. Geng and Q. Zhang, *ChemElectroChem*, 2019, **6**, 3648–3656.
32 Q. S. Fu, J. Wen, N. Zhang, L. L. Wu, M. Y. Zhang, S. Y. Lin, H. Gao and X. T. Zhang, *RSC Adv.*, 2017, **7**, 11998–12005.
33 C. Chen, M. Boota, X. Q. Xie, M. Q. Zhao, B. Anasori, C. E. Ren, L. Miao, J. J. Jiang and Y. Gogotsi, *J. Mater. Chem. A*, 2017, **5**, 5260–5265.
34 T. P. Nguyen, P. L. Rendu, P. D. Long and S. A. De Vos, *Surf. Coat. Technol.*, 2004, **180**, 646–649.
35 D. Yoo, J. Kim, S. H. Lee, W. Cho, H. H. Choi, F. S. Kim and J. H. Kim, *J. Mater. Chem. A*, 2015, **3**, 6526–6533.
36 D. Su, M. Cortie, H. Fan and G. X. Wang, *Adv. Mater.*, 2017, **29**, 1700587.
37 S. Garreau, G. Louarn, J. P. Buisson, G. Froyer and S. Lefrant, *Macromolecules*, 1999, **32**, 6807–6812.
38 Y. Q. Liu, B. Weng, J. M. Razal, Q. Xu, C. Zhao, Y. Y. Hou, S. Seyedin, R. Jalili, G. G. Wallace and J. Chen, *Sci. Rep.*, 2015, **5**, 17045.
39 G. S. Gund, J. H. Park, R. Harpalsinh, M. Kota, J. H. Shin, T. Kim, Y. Gogotsi and H. S. Park, *Joule*, 2019, **3**, 1–13.
40 L. Li, M. Y. Zhang, X. T. Zhang and Z. G. Zhang, *J. Power Sources*, 2017, **364**, 234–241.
41 M. Wang, M. X. Zhou, L. Zhu, Q. F. Li and C. Jiang, *Sol. Energy*, 2016, **129**, 175–183.
42 M. H. Lee, L. X. Chen, N. Li and F. R. Zhu, *J. Mater. Chem. A*, 2017, **5**, 10555–10561.